AFRL-AFOSR-UK-TR-2014-0028

High Order Methods for Compressible Viscous Flow on Unstructured Meshes: New Discretization Techniques and Algorithms

Dr. Georg May

RWTH Aachen University
Aachen Institute for Advanced Study in
Computational Engineering Science
Templergraben 55
Aachen 52074 Germany

EOARD Grant 08-3060

Report Date: February 2014

Final Report from 15 October 2008 to 30 August 2013

Air Force Research Laboratory
Air Force Office of Scientific Research
European Office of Aerospace Research and Development
Unit 4515, APO AE 09421-4515

REPORT DOCUMENTATION PAGE

Form Approved OMB No. 0704-0188

1. REPORT DATE *(DD-MM-YYYY)*	2. REPORT TYPE	3. DATES COVERED *(From – To)*
02 February 2014	Final Report	15 October 2008 – 30 August 2013

4. TITLE AND SUBTITLE

High Order Methods for Compressible Viscous Flow on Unstructured Meshes: New Discretization Techniques and Algorithms

5a. CONTRACT NUMBER

FA8655-08-1-3060

5b. GRANT NUMBER

Grant 08-3060

5c. PROGRAM ELEMENT NUMBER

61102F

6. AUTHOR(S)

Dr. Georg May

5d. PROJECT NUMBER

5d. TASK NUMBER

5e. WORK UNIT NUMBER

7. PERFORMING ORGANIZATION NAME(S) AND ADDRESS(ES)
RWTH Aachen University
Aachen Institute for Advanced Study in Computational Engineering Science
Templergraben 55
Aachen 52074 Germany

8. PERFORMING ORGANIZATION REPORT NUMBER

N/A

9. SPONSORING/MONITORING AGENCY NAME(S) AND ADDRESS(ES)

EOARD
Unit 4515
APO AE 09421-4515

10. SPONSOR/MONITOR'S ACRONYM(S)

AFRL/AFOSR/IOE (EOARD)

11. SPONSOR/MONITOR'S REPORT NUMBER(S)

AFRL-AFOSR-UK-TR-2014-0028

12. DISTRIBUTION/AVAILABILITY STATEMENT

Distribution A: Approved for public release; distribution is unlimited.

13. SUPPLEMENTARY NOTES

14. ABSTRACT

The present project has been initiated with the aim to produce a solution methodology for high order discretization of compressible flow problems that substantially meets industry standards in terms of efficiency and robustness. The approach is two-pronged: Both discretization methods and solution techniques for the arising nonlinear systems of equations are addressed.

This report focuses on the results achieved during the most recent no-cost extension of the project. It is mostly centered around novel discretization methods, in particular hybridized DG schemes. During the current funding phase, we have further developed our hybridized DG discretization method for compressible flow simulation.

15. SUBJECT TERMS

EOARD, Spectral Methods, Computational Fluid Dynamics (CFD)

16. SECURITY CLASSIFICATION OF:			17. LIMITATION OF ABSTRACT	18, NUMBER OF PAGES	19a. NAME OF RESPONSIBLE PERSON
a. REPORT	b. ABSTRACT	c. THIS PAGE			Gregg Abate
UNCLAS	UNCLAS	UNCLAS	SAR	25	19b. TELEPHONE NUMBER *(Include area code)* +44 (0)1895 616021

Performance Report

Grant No. FA8655-08-1-3060

submitted to Program Manager
Gregg Abate
European Office of Aerospace Research and Development

High Order Methods for Compressible Viscous Flow on Unstructured Meshes: New Discretization Techniques and Algorithms

Febrary 2014

Prof. Georg May
Principal Investigator
Aachen Institute for Advanced Study in Computational Engineering Science
RWTH Aachen University

1 Summary

The present project has been initiated with the aim to produce a solution methodology for high-order discretization of compressible flow problems that substantially meets industry standards in terms of efficiency and robustness. The approach is two-pronged: Both discretization methods and solution techniques for the arising nonlinear systems of equations are addressed.

This report focuses on the results achieved during the most recent no-cost extension of the project. It is mostly centered around novel discretization methods, in particular hybridized DG schemes. During the current funding phase, we have further developed our hybridized DG discretization method for compressible flow simulation.

Hybridization has been identified a potential breakthrough technology allowing one to reduce the number of globally coupled degrees of freedom (DOFs) very significantly: Using polynomials or order m with conventional discretization, globally coupled DOFs grow as m^3 and m^2 in two and three dimensions, respectively, while for a hybridized discretization this reduces to m^2 and m. This is obviously very significant for both computational efficiency, and storage requirements, which has been recognized as a major bottleneck for implicit solution methodologies with high-order methods. Among the highlights that will be exposed in more detailed in the technical section of this report are

- Implementation and validation of shock capturing capability
- Target-based hp-adaptation techniques

During the most recent funding period, research partially funded by this project has been presented at

- World Congress on Computational mechanics, July 2012, Sao Paulo, Brazil
- ECCOMAS congress on computational methods in applied sciences and engineering, September 2012, Vienna, Austria
- International Workshop on High-Order CFD Methods, May 2013, Cologne, Germany

An updated list of published results, covering the entire funding period, which acknowledge support from the current grant is given below:

- hybridized DG schemes, including target-based adaptation via adjoint equation [6, 7, 8]
- Stable high-order Spectral Difference method for hyperbolic conservation laws on triangules [1]
- Multilevel methods for solution of the Euler equations [5];
- Matrix-free solution methods for implicit relaxation schemes in response to the extreme storage requirement of implicit relaxation methods for high-order discretization [5, 3, 2];
- Equivalence between Spectral Difference (SD) and nodal Discontinuous Galerkin (DG) schemes [4];

Contents

List of Figures

List of Tables

2 Governing Equations

We consider systems of partial differential equations

$$\boldsymbol{\nabla} \cdot (\mathbf{f}_c(w) - \mathbf{f}_v(w, \boldsymbol{\nabla} w)) = s\,(w, \boldsymbol{\nabla} w) \tag{1}$$

with convective fluxes $\mathbf{f}_c : \mathbb{R}^m \to \mathbb{R}^{m\times d}$ and diffusive fluxes $\mathbf{f}_v : \mathbb{R}^m \times \mathbb{R}^{m\times d} \to \mathbb{R}^{m\times d}$, and a state-dependent source term $s : \mathbb{R}^m \times \mathbb{R}^{m\times d} \to \mathbb{R}^m$. Potentially, some of these quantities could be zero. We denote the spatial dimension by d and the number of conservative variables by m.

2.1 Two-Dimensional Euler Equations

The Euler equations are given in conservative form as

$$\boldsymbol{\nabla} \cdot \mathbf{f}_c(w) = 0 \tag{2}$$

with the vector of conserved variables

$$w = (\rho, \rho\mathbf{v}, E)^T \tag{3}$$

where ρ is the density, $\mathbf{v}$ is the velocity vector $\mathbf{v} := (v_x, v_y)^T$, and E the total energy. The convective flux is given by

$$\mathbf{f}_c = (\rho\mathbf{v}, p\,\mathbf{Id} + \mathbf{v} \otimes \mathbf{v}, \mathbf{v}(E + p))^T. \tag{4}$$

Pressure is related to the conservative flow variables w by the equation of state

$$p = (\gamma - 1)\left(E - \frac{1}{2}\rho\mathbf{v} \cdot \mathbf{v}\right) \tag{5}$$

where $\gamma = c_p/c_v$ is the ratio of specific heats, generally taken as 1.4 for air.

Along wall boundaries we apply the slip boundary condition

$$v_n(w) := \mathbf{v} \cdot \mathbf{n} = 0. \tag{6}$$

We also define a boundary function which satisfies $v_n(w_{\partial\Omega}(w)) = 0$ as

$$w_{\partial\Omega}(w) = \begin{pmatrix} 1 & 0 & 0 & 0 \\ 0 & 1 - n_x^2 & -n_x n_y & 0 \\ 0 & -n_x n_y & 1 - n_y^2 & 0 \\ 0 & 0 & 0 & 1 \end{pmatrix} w. \tag{7}$$

At the far-field can be realized with the aid of characteristic upwinding (exposition omitted)

2.2 Two-Dimensional Navier-Stokes Equations

The Navier-Stokes equations in conservative form are given by

$$\boldsymbol{\nabla} \cdot (\mathbf{f}_c(w) - \mathbf{f}_v(w, \boldsymbol{\nabla} w)) = 0. \tag{8}$$

The convective part $\mathbf{f}_c$ of the Navier-Stokes equations coincides with the Euler equations. The viscous flux is given by

$$\mathbf{f}_v = (\mathbf{0}, \boldsymbol{\tau}, \boldsymbol{\tau}\mathbf{v} + k\boldsymbol{\nabla} T)^T. \tag{9}$$

The temperature is defined via the ideal gas law

$$T = \frac{\mu\gamma}{k \cdot \mathrm{Pr}} \left(\frac{E}{\rho} - \frac{1}{2}\mathbf{v}\cdot\mathbf{v} \right) = \frac{1}{(\gamma-1)c_v}\frac{p}{\rho} \tag{10}$$

where $\mathrm{Pr} = \frac{\mu c_p}{k}$ is the Prandtl number, which for air at moderate conditions can be taken as a constant with a value of $\mathrm{Pr} \approx 0.72$. k denotes the thermal conductivity coefficient. For a Newtonian fluid, the stress tensor is defined as

$$\boldsymbol{\tau} = \mu \left(\boldsymbol{\nabla}\mathbf{v} + (\boldsymbol{\nabla}\mathbf{v})^T - \frac{2}{3}(\boldsymbol{\nabla}\cdot\mathbf{v})\,\mathbf{Id} \right). \tag{11}$$

The variation of the molecular viscosity μ as a function of temperature is determined by Sutherland's law as

$$\mu = \frac{C_1 T^{3/2}}{T + C_2} \tag{12}$$

with $C_1 = 1.458 \times 10^{-6}\,\frac{\mathrm{kg}}{\mathrm{ms}\sqrt{\mathrm{K}}}$ and $C_2 = 110.4\,\mathrm{K}$.

Along wall boundaries, we apply the no-slip boundary condition, i.e.

$$\mathbf{v} = \mathbf{0} \tag{13}$$

with corresponding boundary function

$$w_{\partial\Omega}(w) = (\rho, 0, 0, E)^T \tag{14}$$

Furthermore, one has to give boundary conditions for the temperature. In the present work we use the adiabatic wall condition, i.e.

$$\boldsymbol{\nabla}T \cdot \mathbf{n} = 0 \tag{15}$$

Combining both no-slip and adiabatic wall boundary conditions, gives a condition for the viscous flux, namely

$$\mathbf{f}_{v,\partial\Omega}\left(w_{\partial\Omega}, \mathbf{q}_{\partial\Omega}\right) = \begin{pmatrix} 0 & \tau_{11} & \tau_{21} & 0 \\ 0 & \tau_{12} & \tau_{22} & 0 \end{pmatrix}^T. \tag{16}$$

3 Discretization

3.1 Notation

We tesselate the domain Ω into a collection of non-overlapping elements, denoted by $\mathcal{T}_h$, such that $\bigcup_{K\in\mathcal{T}_h} K = \Omega$. For the element edges we consider two different kinds of sets, $\partial\mathcal{T}_h$ and Γ_h, which are element-oriented and edge-oriented, respectively.

$$\partial\mathcal{T}_h := \{\ \partial K \backslash \partial\Omega\ :\ K \in \mathcal{T}_h\ \}, \tag{17}$$

$$\Gamma_h := \{\ e\ :\ e = K \cap K' \text{ for } K, K' \in \mathcal{T}_h; \mathrm{meas}_{d-1}(e) \neq 0\ \}. \tag{18}$$

The first is the collection of all element boundaries, which means that every edge appears twice. The latter, however, includes every edge just once. The reason for this distinction will become clear later. Please note that neither of these sets shall include edges lying on the domain boundary; the set of boundary edges is denoted by Γ_h^b.

We denote by $\Pi^p(D)$ the set of polynomials of degree at most p on some domain D. We will need discontinuous function spaces for the domain and the mesh skeleton:

$$\mathbf{V}_h = \{v \in L^2(\Omega) \ : v|_K \ \in \Pi^{p_K}(K), \quad K \in \mathcal{T}_h\}^{m\times d} \tag{19}$$

$$W_h = \{w \in L^2(\Omega) \ : w|_K \in \Pi^{p_K}(K), \quad K \in \mathcal{T}_h\}^{m} \tag{20}$$

$$M_h = \{\mu \in L^2(\Gamma_h) : \mu|_e \ \in \Pi^{p_e}(e), \qquad e \ \in \Gamma_h\}^{m}. \tag{21}$$

Thus, $\mathbf{v} \in \mathbf{V}_h$, $w \in W_h$ and $\mu \in M_h$ are piecewise polynomials of degree p which can be discontinuous across edges (for $\mathbf{v}$, w) or vertices (for μ), respectively.

Usually, the polynomial degree between elements and interfaces does not vary. In the case of varying polynomial degrees p_{K^-} and p_{K^+}, we choose the polynomial degree for the interface $e = K^- \cap K^+$ as $p_e = \max\{p_{K^-}, p_{K^+}\}$.

We distinguish between element-oriented inner products (defined with $\mathcal{T}_h$) and edge-oriented inner products (defined with Γ_h)

$$(v,w)_{\mathcal{T}_h} := \sum_{K\in\mathcal{T}_h} \int_K vw \,\mathrm{d}\mathbf{x}, \qquad (\mathbf{v},\mathbf{w})_{\mathcal{T}_h} := \sum_{K\in\mathcal{T}_h} \int_K \mathbf{v}\cdot\mathbf{w} \,\mathrm{d}\mathbf{x}, \tag{22}$$

$$\langle v,w\rangle_{\partial\mathcal{T}_h} := \sum_{K\in\mathcal{T}_h} \int_{\partial K} vw \,\mathrm{d}\sigma, \qquad \langle v,w\rangle_{\Gamma_h} := \sum_{e\in\Gamma_h} \int_e vw \,\mathrm{d}\sigma. \tag{23}$$

3.2 Weak Formulation

We can rewrite general convection-diffusion equations as a first-order system by introducing an additional unknown representing the gradient of the solution

$$\begin{aligned} \mathbf{q} &= \boldsymbol{\nabla} w \\ \boldsymbol{\nabla}\cdot(\mathbf{f}_c(w) - \mathbf{f}_v(w,\mathbf{q})) &= s(w,\mathbf{q}). \end{aligned} \tag{24}$$

By multiplying the strong, mixed form (24) with appropriate test functions $(\boldsymbol{\tau}_h, \varphi_h) \in \mathbf{V}_h \times W_h$ and integrating by parts, we obtain a standard DG discretization in mixed formulation of the problem, i.e.:

Find $(\mathbf{q}_h, w_h) \in \mathbf{V}_h \times W_h$ s.t. $\forall(\boldsymbol{\tau}_h, \varphi_h) \in \mathbf{V}_h \times W_h$

$$0 = \ \mathcal{N}_h^{\mathrm{DG}}(\mathbf{q}_h, w_h; \boldsymbol{\tau}_h, \varphi_h) \tag{25}$$

$$:= \ (\boldsymbol{\tau}_h, \mathbf{q}_h)_{\mathcal{T}_h} + (\boldsymbol{\nabla}\cdot\boldsymbol{\tau}_h, w_h)_{\mathcal{T}_h} - \langle \boldsymbol{\tau}_h\cdot\mathbf{n}, \widehat{w}\rangle_{\partial\mathcal{T}_h} \tag{26}$$

$$- (\boldsymbol{\nabla}\varphi_h, \mathbf{f}_c(w_h) - \mathbf{f}_v(w_h,\mathbf{q}_h))_{\mathcal{T}_h} - (\varphi_h, s(w_h,\mathbf{q}_h))_{\mathcal{T}_h} + \left\langle \varphi_h, \widehat{f_c} - \widehat{f_v}\right\rangle_{\partial\mathcal{T}_h} \tag{27}$$

$$+ \mathcal{N}_{h,\partial\Omega}^{\mathrm{DG}}(\mathbf{q}_h, w_h; \boldsymbol{\tau}_h, \varphi_h) + \mathcal{N}_{h,\mathrm{sc}}^{\mathrm{DG}}(\mathbf{q}_h, w_h; \varphi_h). \tag{28}$$

Here the numerical trace $\widehat{w}$ and the numerical fluxes $\widehat{f_c}, \widehat{f_v}$ have to be chosen appropriately to define a stable and consistent method. Furthermore, the boundary conditions, here denoted by $\mathcal{N}_{h,\partial\Omega}^{\mathrm{DG}}(\mathbf{q}_h, w_h; \boldsymbol{\tau}_h, \varphi_h)$, have to be discretized appropriately.

In contrast to a DG discretization, where the numerical trace $\widehat{w}$ is defined explicitly in terms of w_h and $\mathbf{q}_h$, it is treated as an additional unknown in an HDG method. This additional unknown is called λ_h and has support on the skeleton of the mesh only In order to close the system the continuity of the numerical fluxes across edges is required in a weak sense, resulting in a third equation.

The weak formulation of the hybrid system, comprised of equations for the gradient $\mathbf{q}_h$, the solution itself w_h and its trace on the mesh skeleton λ_h, is then given by:

Find $(\mathbf{q}_h, w_h, \lambda_h) \in \mathbb{X}_h := \mathbf{V}_h \times W_h \times M_h$ s.t. $\forall (\boldsymbol{\tau}_h, \varphi_h, \mu_h) \in \mathbb{X}_h$

$$
\begin{aligned}
0 = \;& \mathcal{N}_h\left(\mathbf{q}_h, w_h, \lambda_h; \boldsymbol{\tau}_h, \varphi_h, \mu_h\right) && (29)\\
:= \;& \left(\boldsymbol{\tau}_h, \mathbf{q}_h\right)_{\mathcal{T}_h} + \left(\boldsymbol{\nabla}\cdot\boldsymbol{\tau}_h, w_h\right)_{\mathcal{T}_h} - \left\langle \boldsymbol{\tau}_h\cdot\mathbf{n}, \lambda_h\right\rangle_{\partial\mathcal{T}_h} && (30)\\
& - \left(\boldsymbol{\nabla}\varphi_h, \mathbf{f}_c(w_h) - \mathbf{f}_v(w_h, \mathbf{q}_h)\right)_{\mathcal{T}_h} - \left(\varphi_h, s(w_h, \mathbf{q}_h)\right)_{\mathcal{T}_h} + \left\langle \varphi_h, \widehat{f_c} - \widehat{f_v}\right\rangle_{\partial\mathcal{T}_h} && (31)\\
& + \mathcal{N}_{h,\partial\Omega}\left(\mathbf{q}_h, w_h; \boldsymbol{\tau}_h, \varphi_h\right) + \mathcal{N}_{h,\mathrm{sc}}\left(\mathbf{q}_h, w_h; \varphi_h\right) && (32)\\
& + \left\langle \mu_h, \left[\!\left[\widehat{f_c} - \widehat{f_v}\right]\!\right]\right\rangle_{\Gamma_h}. && (33)
\end{aligned}
$$

The terms tested against $\boldsymbol{\tau}_h$ and φ_h are called local solvers, meaning they do not depend on the solution within neighboring elements but only on the trace of the solution which is approximated by λ_h. The coupling between elements is then introduced by weakly enforcing the normal continuity of the numerical fluxes across interfaces.

We choose numerical fluxes comparable to the Lax-Friedrich flux and to the LDG flux for the convective and diffusive flux, respectively, i.e.

$$\widehat{f_c}\left(\lambda_h, w_h\right) = \mathbf{f}_c\left(\lambda_h\right)\cdot\mathbf{n} - \alpha_c\left(\lambda_h - w_h\right) \tag{34}$$

$$\widehat{f_v}\left(\lambda_h, w_h, \mathbf{q}_h\right) = \mathbf{f}_v\left(\lambda_h, \mathbf{q}_h\right)\cdot\mathbf{n} + \alpha_v\left(\lambda_h - w_h\right) \tag{35}$$

which can be combined into

$$\widehat{f_c} - \widehat{f_v} = \left(\mathbf{f}_c\left(\lambda_h\right) - \mathbf{f}_v\left(\lambda_h, \mathbf{q}_h\right)\right)\cdot\mathbf{n} - \left(\alpha_c + \alpha_v\right)\left(\lambda_h - w_h\right). \tag{36}$$

The stabilization introduced can be given by a tensor; in our work, however, we restrict ourselves to a constant scalar $\alpha = \alpha_c + \alpha_v$ which seems to be sufficient for a wide range of test cases.

3.2.1 Boundary Conditions

In order to retrieve an adjoint-consistent scheme, special care has to be taken when discretizing the boundary conditions (see [7]). The boundary conditions have to be incorporated by using the boundary states $w_{\partial\Omega}\left(w_h\right)$ and gradients $\mathbf{q}_{\partial\Omega}\left(w_h, \mathbf{q}_h\right)$, i.e.

$$
\begin{aligned}
\mathcal{N}_{h,\partial\Omega}\left(\mathbf{q}_h, w_h; \boldsymbol{\tau}_h, \varphi_h\right) := \;& \left\langle \boldsymbol{\tau}_h\cdot\mathbf{n}, w_{\partial\Omega}\right\rangle_{\Gamma_h^b}\\
& + \left\langle \varphi_h, \left(\mathbf{f}_c\left(w_{\partial\Omega}\right) - \mathbf{f}_v\left(w_{\partial\Omega}, \mathbf{q}_{\partial\Omega}\right)\right)\cdot\mathbf{n}\right\rangle_{\Gamma_h^b}.
\end{aligned}
$$

We would like to emphasize that λ_h does not occur in this boundary term.

3.2.2 Shock-Capturing

We adopt a shock-capturing term, where an artificial viscosity term, given by $\boldsymbol{\nabla}\cdot\left(\epsilon\left(w, \boldsymbol{\nabla}w\right)\boldsymbol{\nabla}w\right)$, is used. The viscosity ϵ is given by the L1-norm of the strong residual $\boldsymbol{\nabla}\cdot\mathbf{f}_c(w)$ in every element. In order to accelerate the convergence of this term to zero with mesh refinement, it is premultiplied with an effective mesh size $\tilde{h}_K := \frac{h_K}{p_K}$. The latter resembles the actual resolution within an element. Furthermore, a user-defined factor ϵ_0 is introduced which can be reliably tuned for a rather large range of test cases. Finally, the artificial viscosity is given by

$$\epsilon|_K := \frac{\epsilon_0 \tilde{h}_K^{2-\beta}}{|K|}\int_K d(w)\,\mathrm{d}\mathbf{x} \tag{37}$$

where the strong residual is given by

$$d(w) := \sum_{i=1}^{m} \left| (\boldsymbol{\nabla} \cdot \mathbf{f}_c(w))_i \right| . \tag{38}$$

In the discretization of this shock-capturing term the interface integral is neglected so that only the volume contribution is considered, i.e.

$$\mathcal{N}_{h,\mathrm{sc}} \left(w_h; \varphi_h \right) := \left(\boldsymbol{\nabla} \varphi_h, \epsilon \left(w_h, \boldsymbol{\nabla} w_h \right) \boldsymbol{\nabla} w_h \right)_{\mathcal{T}_h} . \tag{39}$$

This obviates the need for introducing $\mathbf{q}_h$ in purely convective problems (e.g. the compressible Euler equations). In the viscous case, where the gradient is explicitly given, $\boldsymbol{\nabla} w_h$ can be replaced by $\mathbf{q}_h$ yielding

$$\mathcal{N}_{h,\mathrm{sc}} \left(\mathbf{q}_h, w_h; \varphi_h \right) := \left(\boldsymbol{\nabla} \varphi_h, \epsilon \left(w_h, \mathbf{q}_h \right) \mathbf{q}_h \right)_{\mathcal{T}_h} . \tag{40}$$

Please note, that this term enters only the local part of the discretization.

3.3 Relaxation

We solve the nonlinear system of equations that defines the HDG method, with a damped Newton-Raphson method. An artificial time is introduced, and we solve at each iteration index n,

$$\left(\varphi_h, \frac{1}{\Delta t^n} \delta w_h^n \right)_{\mathcal{T}_h} + \mathcal{N}_h' \left[\mathbb{x}_h^n \right] \left(\delta \mathbb{x}_h^n; \mathbb{y}_h \right) = -\mathcal{N}_h \left(\mathbb{x}_h^n; \mathbb{y}_h \right) \quad \forall \mathbb{y}_h \in \mathbb{X}_h. \tag{41}$$

Please note that by choosing $\Delta t^n \to \infty$, a pure Newton-Raphson method is obtained. Usually the time step is kept finite for a few initial steps to ensure stability. As soon as the residual is lower than a certain threshold, i.e. the current approximation $\mathbb{x}_h^n$ is thought to be sufficiently close to the solution $\mathbb{x}_h$, we let the time step go towards infinity.

3.4 Hybridization

Using an appropriate polynomial expansion for $\delta \mathbf{q}_h$, δw_h and $\delta \lambda_h$, the linearized global system is given in matrix form as

$$\begin{bmatrix} A & B & R \\ C & D & S \\ L & M & N \end{bmatrix} \begin{bmatrix} \delta Q \\ \delta W \\ \delta \Lambda \end{bmatrix} = \begin{bmatrix} F \\ G \\ H \end{bmatrix} \tag{42}$$

where the vector $[\delta Q, \delta W, \delta \Lambda]^T$ contains the expansion coefficients of $\delta \mathbf{x}_h$ with respect to the chosen basis.

In order to carry on with the derivation of the hybridized method, we want to formulate that system in terms of $\delta \Lambda$ only. Therefore we split it into

$$\begin{bmatrix} A & B \\ C & D \end{bmatrix} \begin{bmatrix} \delta Q \\ \delta W \end{bmatrix} = \begin{bmatrix} F \\ G \end{bmatrix} - \begin{bmatrix} R \\ S \end{bmatrix} \delta \Lambda \tag{43}$$

and

$$\begin{bmatrix} L & M \end{bmatrix} \begin{bmatrix} \delta Q \\ \delta W \end{bmatrix} + N \delta \Lambda = H. \tag{44}$$

Substituting Eq. (43) into Eq. (44) yields the hybridized system

$$\left(N - \begin{bmatrix} L & M \end{bmatrix} \begin{bmatrix} A & B \\ C & D \end{bmatrix}^{-1} \begin{bmatrix} R \\ S \end{bmatrix} \right) \delta \Lambda = H - \begin{bmatrix} L & M \end{bmatrix} \begin{bmatrix} A & B \\ C & D \end{bmatrix}^{-1} \begin{bmatrix} F \\ G \end{bmatrix} \tag{45}$$

The workflow is as follows: First, the hybridized system is assembled and then being solved for $\delta\Lambda$. Subsequently, δQ and δW can be reconstructed inside the elements via Eq. (43). It is very important to note that it is not necessary to solve the large system given by Eq. (43). In fact, the matrix in Eq. (43) can be reordered to be block diagonal. Each of these blocks is associated to one element. Thus, both the assembly of the hybridized matrix in Eq. (45) and the reconstruction of δQ and δW can be done in an element-wise fashion. In order to save computational time, the solutions to Eq. (43) can be saved after the assembly of the hybridized system and reused during the reconstruction of δQ and δW.

The hybridized matrix is a $n_f \times n_f$ block matrix, where $n_f = |\Gamma_h|$ is the number of interior edges. In each block row there is one block on the diagonal and $2d$ off-diagonal blocks in the case of simplex elements. These blocks represent the edges of the neighboring elements of one edge. Each block is dense and has $\mathcal{O}\left(m^2 \cdot p^{2(d-1)}\right)$ entries. Please recall that p is the polynomial degree of the ansatz functions, d is the spatial dimension of the domain Ω and m is the number of partial differential equations ($m = 4$ for the 2-dimensional Euler or Navier-Stokes equations). This structure is very similar to that of a normal DG discretization, whereas the blocks in the latter have $\mathcal{O}\left(m^2 \cdot p^{2d}\right)$ entries and thus are considerably bigger for higher polynomial order p.

4 Adaptation Procedure

In the context of adjoint-based (also referred to as target- or output-based) error estimation, one is interested in quantifying the error of a specific target functional $J_h : \mathbb{X}_h \to \mathbb{R}$, i.e.

$$e_h := J_h(\mathbb{x}) - J_h(\mathbb{x}_h), \tag{46}$$

where $\mathbb{x}_h$ is the approximation to $\mathbb{x}$ in $\mathbb{X}_h$. This target functional can, for example, represent lift or drag coefficients in aerospace applications. For the derivation of the adjoint-based error estimate we expand the target functional in a Taylor series as follows

$$J_h(\mathbb{x}) - J_h(\mathbb{x}_h) = J_h'[\mathbb{x}_h](\mathbb{x} - \mathbb{x}_h) + \mathcal{O}\left(\|\mathbb{x} - \mathbb{x}_h\|^2\right). \tag{47}$$

We proceed in a similar manner with the error in the residual, i.e.

$$\mathcal{N}_h(\mathbb{x}; \mathbb{y}_h) - \mathcal{N}_h(\mathbb{x}_h; \mathbb{y}_h) = \mathcal{N}_h'[\mathbb{x}_h](\mathbb{x} - \mathbb{x}_h; \mathbb{y}_h) + \mathcal{O}\left(\|\mathbb{x} - \mathbb{x}_h\|^2\right). \tag{48}$$

As our discretization is consistent the first term $\mathcal{N}_h(\mathbb{x}; \mathbb{y}_h)$ vanishes.

Substituting Eq. (48) into Eq. (47) and neglecting the quadratic terms yields

$$e_h \approx \eta := -\mathcal{N}_h(\mathbb{x}_h; \mathbb{z}_h) \tag{49}$$

where $\mathbb{z}_h$ is defined by the so-called adjoint equation

$$\mathcal{N}_h'[\mathbb{x}_h](\mathbb{y}_h; \mathbb{z}_h) = J_h'[\mathbb{x}_h](\mathbb{y}_h) \qquad \forall \mathbb{y}_h \in \widetilde{\mathbb{X}}_h. \tag{50}$$

The adjoint solution $\mathbb{z}_h = \left(\widetilde{q}_h, \widetilde{w}_h, \widetilde{\lambda}_h\right) \in \widetilde{\mathbb{X}}_h$ represents the link between variations in the residual and in the target functional.

The global error estimate η can then be restricted to a single element to yield a local indicator to drive an adaptation procedure, i.e.

$$\eta_K := \left|\mathcal{N}_h(\mathbf{q}_h, w_h, \lambda_h; \widetilde{\mathbf{q}}_h, \widetilde{w}_h, 0)\big|_K\right|. \tag{51}$$

Here, we want to emphasize that, in contrast to the global error estimate, we ignore the contribution of the hybrid adjoint variable $\widetilde{\lambda}_h$. We found that by taking the whole adjoint into account, jumps across element interfaces were overly penalized. This deserves a more in-depth analysis.

Please note, that the functionals $\mathcal{N}_h$ and J_h and their jacobians have to be evaluated in a somewhat richer space than $\mathbb{X}_h$, namely $\widetilde{\mathbb{X}}_h \supset \mathbb{X}_h$. Otherwise the weighted residual $\mathcal{N}_h(\mathbb{x}_h; \mathbb{z}_h)$ would be identical zero as

$$\mathcal{N}_h(\mathbb{x}_h; \mathbb{y}_h) = 0 \qquad \forall \mathbb{y}_h \in \mathbb{X}_h. \tag{52}$$

This can be achieved by either mesh refinement or a higher polynomial degree of the ansatz functions. In our setting, especially when using a hierarchical basis, the latter is advantageous with respect to implementational effort and efficiency.

4.1 Hybridization

In matrix form, the adjoint system (see Eq. (50)) reads as follows

$$\begin{bmatrix} A & B & R \\ C & D & S \\ L & M & N \end{bmatrix}^T \begin{bmatrix} \widetilde{Q} \\ \widetilde{W} \\ \widetilde{\Lambda} \end{bmatrix} = \begin{bmatrix} \widetilde{F} \\ \widetilde{G} \\ \widetilde{H} \end{bmatrix} \tag{53}$$

Please note, that in our formulation $\widetilde{H} = 0$ as λ_h is not defined on the boundary and thus the target functional depends only on w_h and q_h.

As the overall structure of the adjoint equation is similar to the primal system (see Eq. (45)), one can also apply static condensation to the adjoint system which then yields its hybridized form:

$$\left(N - \begin{bmatrix} L & M \end{bmatrix} \begin{bmatrix} A & B \\ C & D \end{bmatrix}^{-1} \begin{bmatrix} R \\ S \end{bmatrix} \right)^T \widetilde{\Lambda} = - \begin{bmatrix} R^T & S^T \end{bmatrix} \begin{bmatrix} A & B \\ C & D \end{bmatrix}^{-T} \begin{bmatrix} \widetilde{F} \\ \widetilde{G} \end{bmatrix}$$

It is interesting to note that the hybridized adjoint system matrix is also the transpose of the hybridized primal system matrix (for a higher polynomial order). This is very beneficial for the implementation as the routines for the assembly of this matrix are already available.

The adjoint solution within each element can then be computed with the aid of the adjoint local system, given by

$$\begin{bmatrix} A & B \\ C & D \end{bmatrix}^T \begin{bmatrix} \widetilde{Q} \\ \widetilde{W} \end{bmatrix} = \begin{bmatrix} \widetilde{F} \\ \widetilde{G} \end{bmatrix} - \begin{bmatrix} L & M \end{bmatrix}^T \widetilde{\Lambda} \tag{54}$$

where the matrix is also the transpose of the primal local matrix (see Eq. (43)).

4.2 Marking Elements for Refinement

After having obtained a localized error estimate, we choose a set of elements to be refined. The aim of our marking strategy is to find the smallest set $\mathcal{M} \subseteq \mathcal{T}_h$ such that the error contributed by this set represents a certain fraction of the total error, i.e.

$$\eta_{\mathcal{M}} \geq (1 - \theta)\, \eta_{\mathcal{T}_H}. \tag{55}$$

The user-defined parameter θ is of course problem dependent. It can, however, be tuned for a big range of test cases. Please note, that we define the error of any subset of $\mathcal{T}_h$ as $\eta^2_{\mathcal{M}} := \sum_{K \in \mathcal{M}} \eta^2_K$.

4.3 Choosing between h- and p-Adaptation

The final step in the adaptation procedure is the decision between mesh refinement and order enrichment. On each element a smoothness sensor is defined as

$$S_K := \frac{(w - w^\star, w - w^\star)_K}{(w, w)_K} \tag{56}$$

where $w^\star$ is the element-wise projection of w to the next smaller polynomial space, given by

$$(\varphi_h, w^\star)_K = (\varphi_h, w)_K \qquad \forall \varphi_h \in \Pi^{p_K - 1}. \tag{57}$$

Hence, $w - w^\star$ represents the higher order components of the solution (see Fig. 1). As we use an hierarchical basis, this projection is very cheap. By introducing a threshold ϵ_S, a decision between mesh-refinement and p-enrichment can be made, i.e.

$$S_K \begin{cases} < \epsilon_S & p\text{-enrichment} \\ \geq \epsilon_S & \text{mesh-refinement} \end{cases} \tag{58}$$

5 Results

In the following we compare our in-house HDG and DG solvers in terms of degrees of freedom and runtime. The DG discretization is based on the Lax-Friedrich and the BR2 fluxes for convective and viscous terms, respectively. Both solvers share the same computational framework, so we believe that our comparison is meaningful.

We apply both solvers to compressible flow problems, including inviscid subsonic and transonic, and subsonic laminar flow. In all cases we show results for pure mesh-adaptation ($p = 1 \dots 4$) and hp-adaptation ($p = 2 \dots 5$).

Please note, that we choose the same relaxation parameters for all test cases. If artificial viscosity is necessary, we use $\epsilon_0 = 0.2$ and $\beta = 0$. The parameters for the adaptation procedure are chosen as $\theta = 0.05$ and $\epsilon_S = 10^{-6}$. This set of parameters seems to be robust for both DG and HDG for a broad range of test cases. In order to approximate the error in drag, reference solutions on hp-adapted meshes with more than $2 \cdot 10^6$ degrees of freedom (please note, that we refer to ndof_w whenever we speak of degrees of freedom in the following as this is a good measure for the resolution) are used.

Before we turn our attention to the adaptive computations, we want to compare runtimes for both methods on a fixed mesh for several polynomial orders. This way, we can a priori learn which improvement can be expected. In Fig. 2 timings for the assembly procedure and the iterative solver are given. We show Euler and a Navier-Stokes computation on a mesh with 2396 elements and 3544 interior faces. We used polynomial orders from $p = 0$ to $p = 6$. We want to emphasize that the necessary Newton and GMRES iterations for both HDG and DG were comparable. As there are more faces than elements, DG is faster than HDG for $p = 0$ and $p = 1$. However, already for $p = 2$ HDG catches up. At $p = 6$ there is a ratio of 2.5 for the Euler test case and 2.1 for the Navier-Stokes test case. For the Euler test case it is interesting to note, that the iterative solver dominates the computational time for DG. For HDG it is the other way around. This has two reasons: firstly, the assembly is more involved due to the local solves; and secondly, the global system is considerably smaller for higher polynomial degree. In the case of a Navier-Stokes computation, the DG assembly takes over the dominating part as the lifting operators are very expensive to compute. The time for the HDG assembly is also increased which is among other things due to the introduction of the gradient. For both HDG and DG, the time spent in the iterative solver is comparable for both Euler and Navier-Stokes.

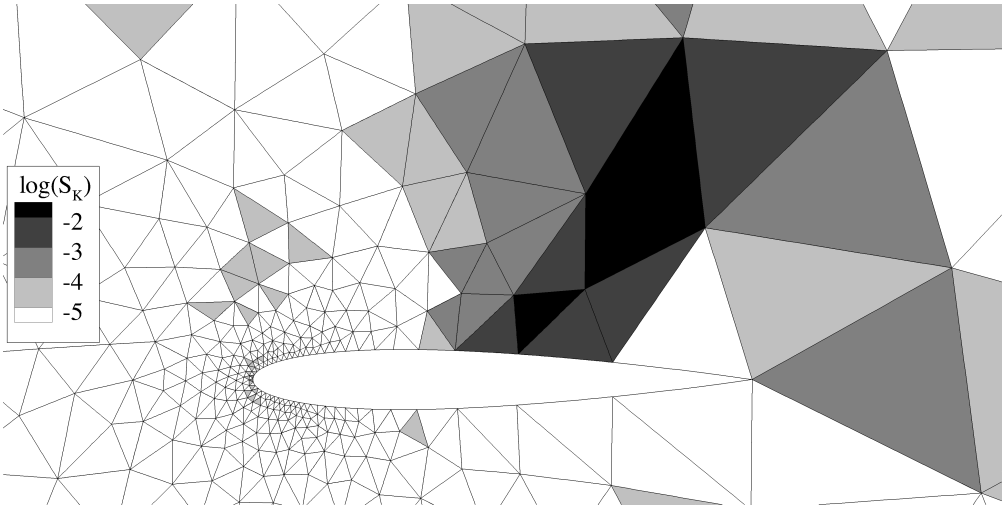

(a) Coarse mesh

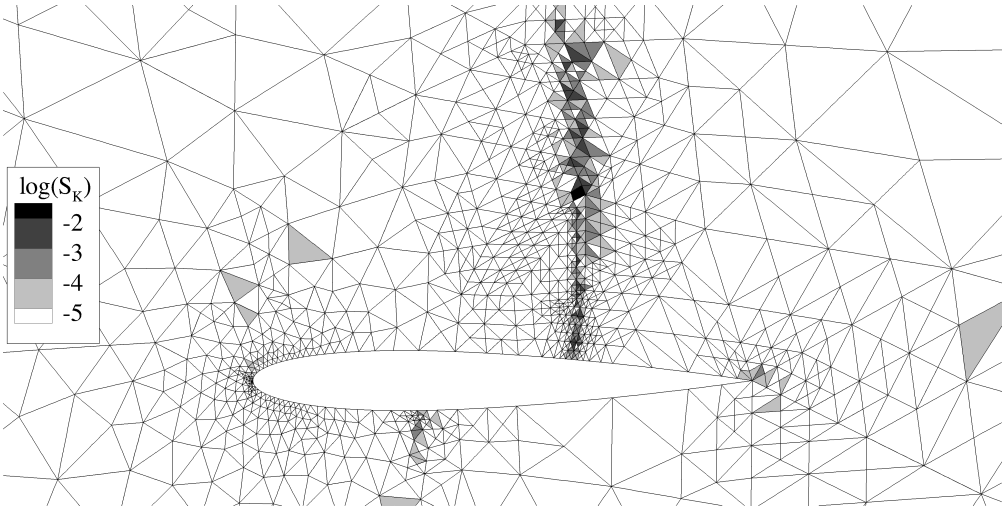

(b) Adapted mesh

Figure 1: Smoothness sensor for a transonic test case

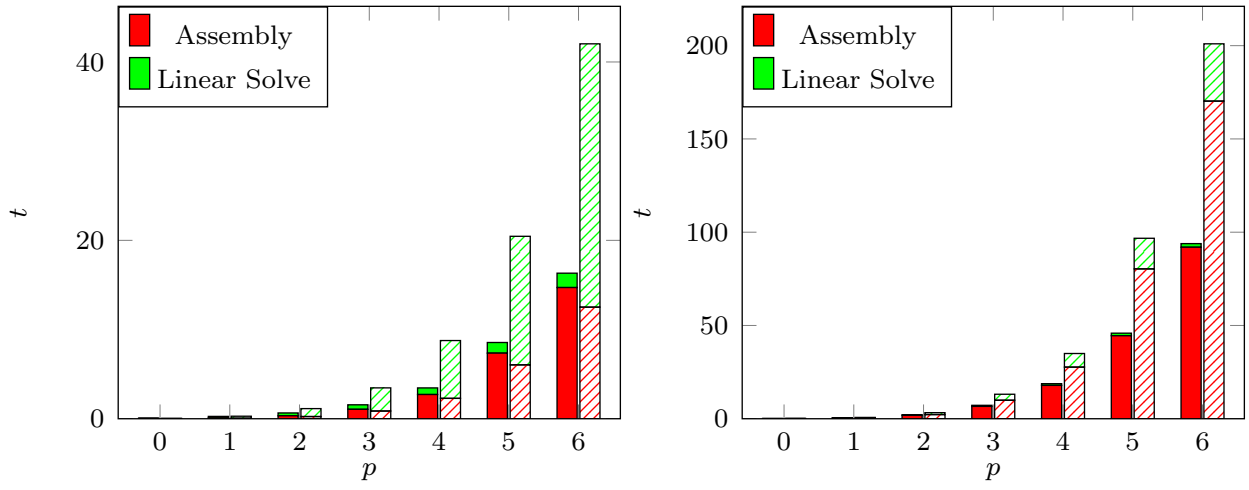

(a) Euler

(b) Navier-Stokes

Figure 2: Runtime comparison of the hybridized and non-hybridized DG method for a fixed mesh and varying polynomial degree (Solid: HDG, Shaded: DG).

5.1 Subsonic Inviscid Flow over the NACA 0012 Airfoil

In the first test case, we consider subsonic inviscid flow over the NACA 0012 airfoil which is defined by

$$y = \pm 0.6 \left(0.2969\sqrt{x} - 0.1260x - 0.3516x^2 + 0.2843x^3 - 0.1015x^4\right) \tag{59}$$

with $x \in [0, 1]$. Using this definition, the airfoil would have a finite trailing edge thickness of .252 %. In order to obtain a sharp trailing edge we modify the x^4 coefficient, i.e.

$$y = \pm 0.6 \left(0.2969\sqrt{x} - 0.1260x - 0.3516x^2 + 0.2843x^3 - 0.1036x^4\right). \tag{60}$$

The flow is characterized by a free stream Mach number of $\mathrm{Ma}_\infty = 0.5$ and an angle of attack of $\alpha = 2°$. In Fig. 3 the baseline mesh for the Euler test cases (subsonic and transonic) can be seen. It consists of 719 elements and its far field is over a 1000 chords away.

Admissible target functionals defined on the boundary for the Euler equations are given by the weighted pressure along wall boundaries, i.e.

$$J(w) = \int_{\partial\Omega} \boldsymbol{\psi} \cdot (p\mathbf{n}) \, \mathrm{d}\sigma \tag{61}$$

where $\mathbf{n}$ is the outward pointing normal. By using $\boldsymbol{\psi} = \frac{1}{C_\infty} (\cos\alpha, \sin\alpha)^T$ or $\boldsymbol{\psi} = \frac{1}{C_\infty} (-\sin\alpha, \cos\alpha)^T$ along wall boundaries and 0 otherwise, the functional represents the pressure drag coefficient c_D or the pressure lift coefficient c_L, respectively. C_∞ is a normalized reference value defined by $C_\infty = \frac{1}{2}\gamma \mathrm{Ma}_\infty^2 p_\infty l$. Here, l is the chord length of the airfoil.

In Fig. 4a, a purely h-adapted mesh can be seen. The most refined regions are the leading and trailing edge. The first is of importance as the flow experiences high gradients towards the stagnation point. Refinement of the latter is necessary due to the sharp trailing edge and the slip-wall boundary conditions. As soon as the error in these two regions is sufficiently low, other elements close to the airfoil get refined as well. For the hp-adapted mesh (see Fig. 4b) the leading and trailing edge are refined as well. All other regions, however, undergo mostly p-enrichment.

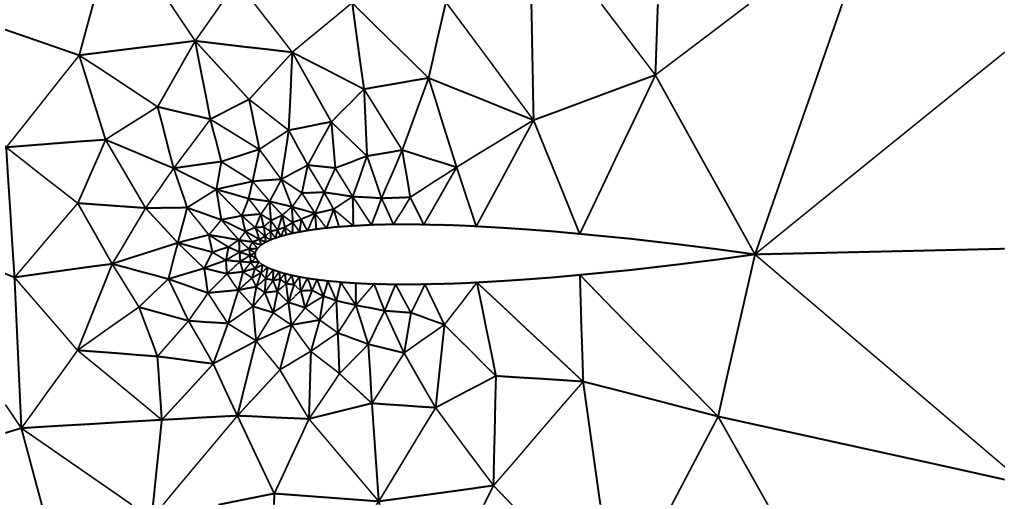

Figure 3: Baseline mesh with 719 elements for inviscid computations

p	1	2	3	4	hp
$t_{\mathrm{DG}}/t_{\mathrm{HDG}}$	1.293	3.799	3.551	3.092	2.209
$n_{\mathrm{nz,DG}}/n_{\mathrm{nz,HDG}}$	1.123	2.150	3.248	4.281	4.601

Table 1: Runtime and nonzero ratios for a fixed error level ($\mathrm{Ma}_\infty = 0.5$, $\alpha = 2°$)

In terms of degrees of freedom, both HDG and DG show similar results. For all computations it takes some adaptations until the critical regions, leading and trailing edge, are resolved. From this point on, one can see the benefit of a higher order discretization: the error drops significantly faster with respect to degrees of freedom and computational time (see Fig. 5 and 6).

In Tbl. 1, we give the runtime ratios for a fixed error level (we always choose the minimum level attained). For $p = 1$, HDG and DG are comparable in both runtime and nonzero entries. From $p = 2$ on, HDG is faster than DG and needs less memories for the global system. Here, it is important to note that the adjoint is approximated with $p + 1$, so that already for lower orders HDG is faster.

5.2 Transonic Inviscid Flow over the NACA 0012 Airfoil

Next, we turn our attention to transonic flow which develops more complex features (e.g. compression shocks) compared to the subsonic regime. The flow is characterized by a free stream Mach number of $\mathrm{Ma}_\infty = 0.8$ and an angle of attack of $\alpha = 1.25°$.

In Fig. 7a a purely h-adapted mesh can be seen. The adjoint sensor detects all regions of relevance for the drag: the upper shock, the leading and trailing edge, and the lower weak shock. Further refinement is added upstream of the shock, where the adjoint has steep gradients and thus needs higher resolution. In the case of hp-adaptation, the mesh-refinement is stronger confined to the shock region and the trailing edge. The other features undergo p-enrichment.

As expected, both methods show a similar accuracy for a given number of degrees of freedom. The computations with $p = 2 \dots 4$ outperform $p = 1$ but are comparable to each other. hp-adaptation shows very good results which is due to the accurate prediction of the solution smoothness (see Fig. 8 and 9).

For this test case, HDG is faster than DG from $p = 1$ on (see Tbl. 2). The hp-adaptive run

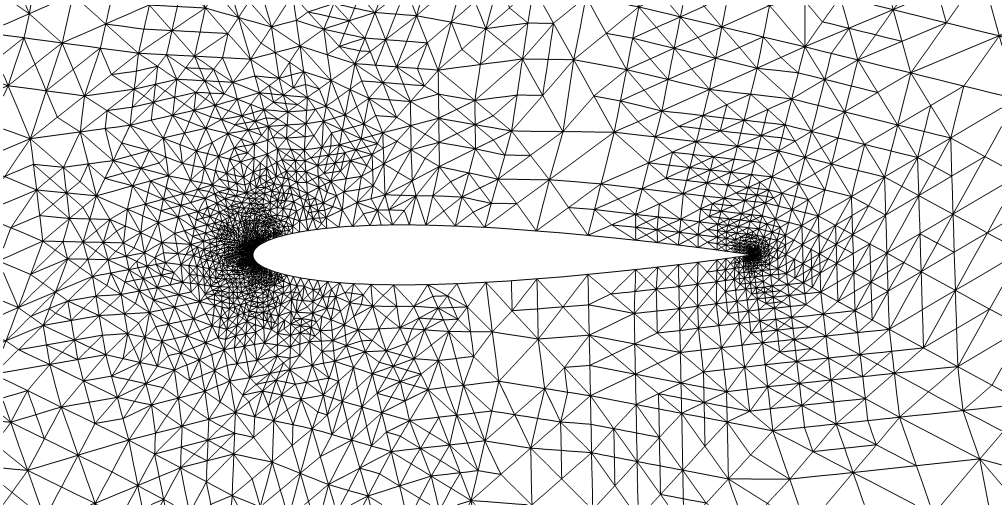

(a) Pure h-adapation ($p = 2$)

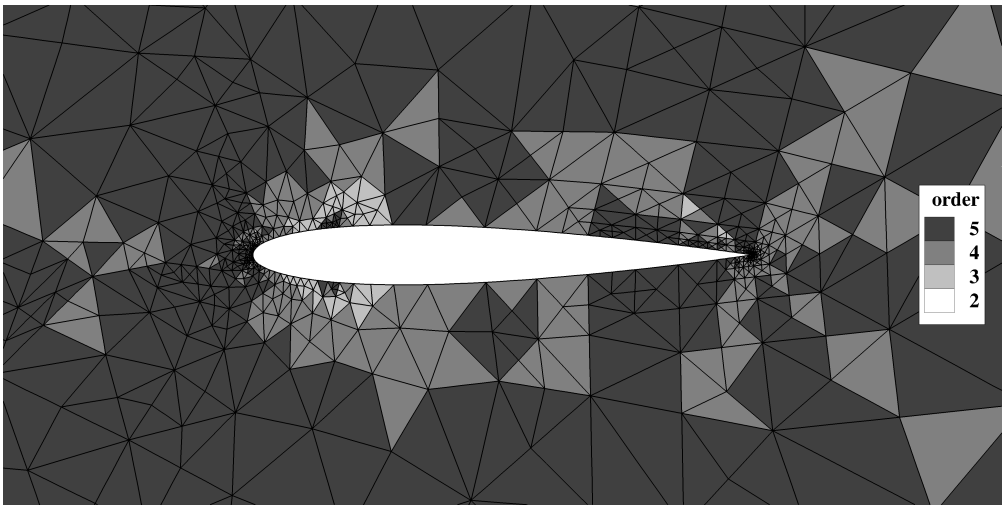

(b) hp-adapation ($p = 2 \dots 5$)

Figure 4: Adapted meshes for the subsonic Euler test case ($\mathrm{Ma}_\infty = 0.5$, $\alpha = 2°$)

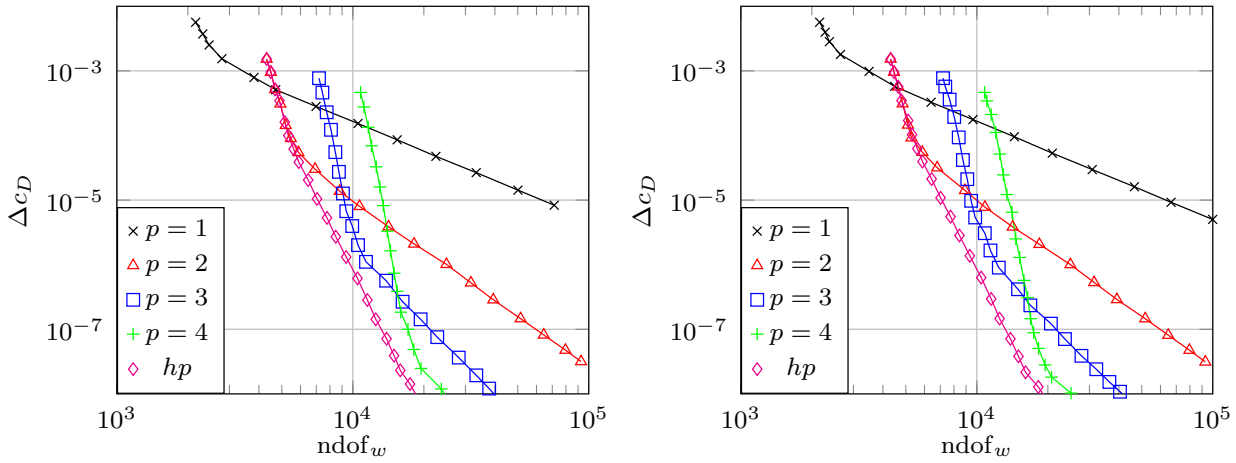

(a) HDG (b) DG

Figure 5: Drag convergence with respect to degrees of freedom ($\text{Ma}_\infty = 0.5$, $\alpha = 2°$)

p	1	2	3	4	hp
$t_{\text{DG}}/t_{\text{HDG}}$	2.636	1.607	2.154	2.362	2.628
$n_{\text{nz,DG}}/n_{\text{nz,HDG}}$	1.237	1.807	3.098	4.437	2.411

Table 2: Runtime and nonzero ratios for a fixed error level ($\text{Ma}_\infty = 0.8$, $\alpha = 1.25°$)

is more than 2.5 times faster. The ratio of necessary nonzero entries attains its highest value for $p = 4$. In the case of hp-adaptation, this ratio is not as high, as in the shock region a lot of elements with $p = 2$ exist.

5.3 Subsonic Laminar Flow over the NACA 0012 Airfoil

Finally, we consider viscous flow in the subsonic regime. The free stream Mach number is $\text{Ma}_\infty = 0.5$, the angle of attack $\alpha = 1°$ and the Reynolds number $\text{Re} = 5000$. Due to the latter, a thin boundary layer develops around the airfoil.

The baseline mesh for the Navier-Stokes test case is more refined around the airfoil such that the boundary layer is correctly captured (see Fig. 10). It consists of 1781 elements and its far field is over a 1000 chords away.

Admissible target functionals defined on the boundary for the Navier-Stokes equations are given by the weighted boundary flux along wall boundaries, i.e.

$$J(w, \nabla w) = \int_{\partial\Omega} \boldsymbol{\psi} \cdot (p\mathbf{n} - \boldsymbol{\tau}\mathbf{n}) \, \mathrm{d}\sigma \tag{62}$$

where $\mathbf{n}$ is the outward pointing normal. Here, ψ is nonzero only on wall boundaries. By using $\boldsymbol{\psi} = \frac{1}{C_\infty}(\cos\alpha, \sin\alpha)^T$ or $\boldsymbol{\psi} = \frac{1}{C_\infty}(-\sin\alpha, \cos\alpha)^T$ along wall boundaries and otherwise 0, the functional represents the viscous drag coefficient c_D or the viscous lift coefficient c_L, respectively.

Both the h-adapted mesh (see Fig. 11a) and the hp-adapted mesh (see Fig. 11b) undergo refinement within the boundary layer and the wake region. The mesh refinement for the hp-adaptive run is however more restricted to the leading edge region where the boundary layer develops. Further downstream, p-enrichment is used as soon as the necessary mesh-resolution is reached.

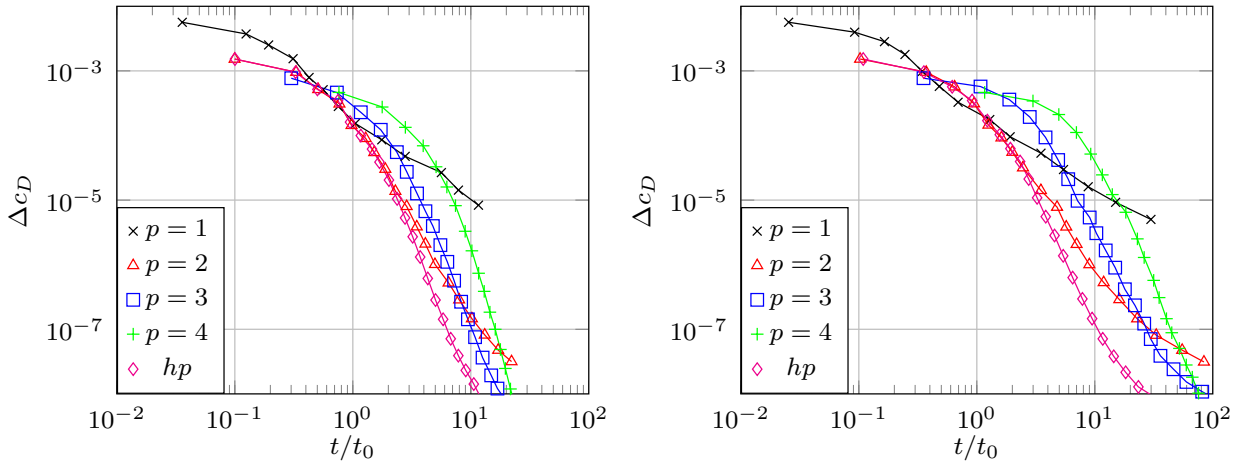

(a) HDG

(b) DG

Figure 6: Drag convergence with respect to time ($\mathrm{Ma}_\infty = 0.5$, $\alpha = 2°$)

p	1	2	3	4	hp
$t_{\mathrm{DG}}/t_{\mathrm{HDG}}$	2.244	2.572	2.397	2.288	3.122
$n_{\mathrm{nz,DG}}/n_{\mathrm{nz,HDG}}$	1.196	2.235	3.472	4.531	3.463

Table 3: Runtime and nonzero ratios for a fixed error level ($\mathrm{Ma}_\infty = 0.5$, $\alpha = 1°$, $\mathrm{Re} = 5000$)

In terms of accuracy versus degrees of freedom, HDG and DG perform comparably well. The higher the polynomial degree the more accurate and efficient the computations are for both HDG and DG (see Fig. 12 and 13). The difference between hp, $p = 3$ and $p = 4$ is not as big, though. This might lead to the conclusion that isotropic mesh refinement is not longer efficiently applicable in cases involving strong gradients. Hence, the efficiency of the adaptation procedure is rather limited by the mesh refinement strategy.

Concerning the timings, we can see a similar trend as in the previous test cases (see Tbl. 3). For $p = 1 \ldots 4$, HDG is more than twice as fast. The hp-adaptive HDG computation is even three times as fast compared to the DG run. From $p = 2$ on, the savings in nonzero entries for HDG become significant.

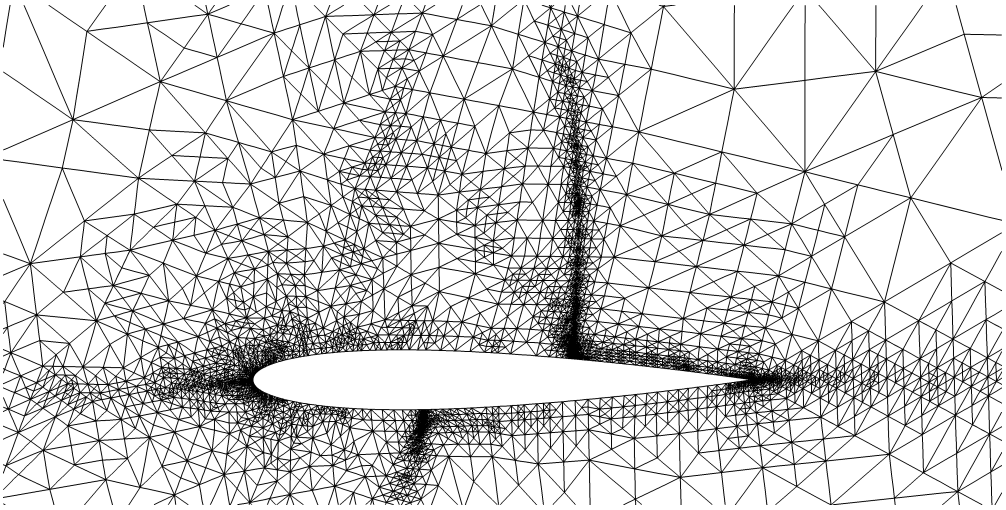

(a) Pure h-adaptation ($p = 2$)

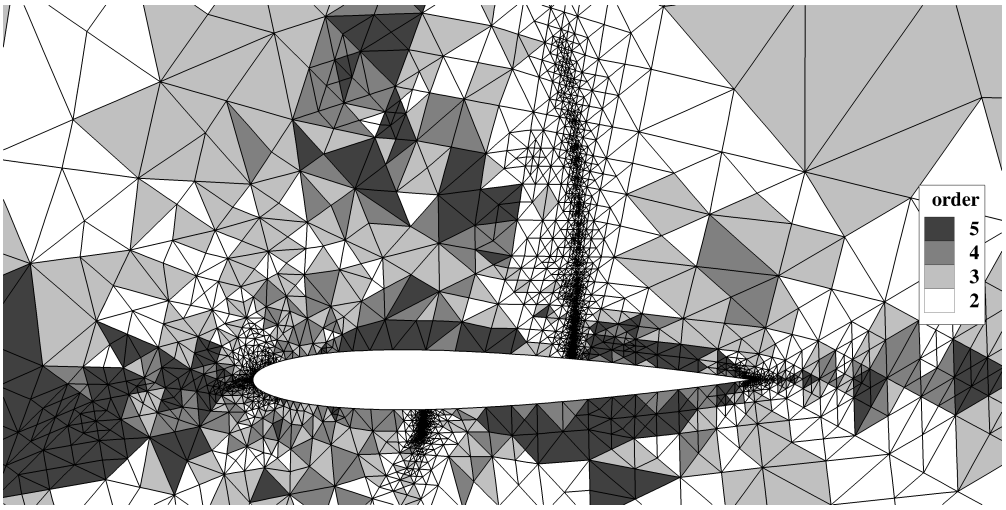

(b) hp-adaptation ($p = 2 \dots 5$)

Figure 7: Adapted meshes for the transonic Euler test case ($\mathrm{Ma}_\infty = 0.8$, $\alpha = 1.25°$)

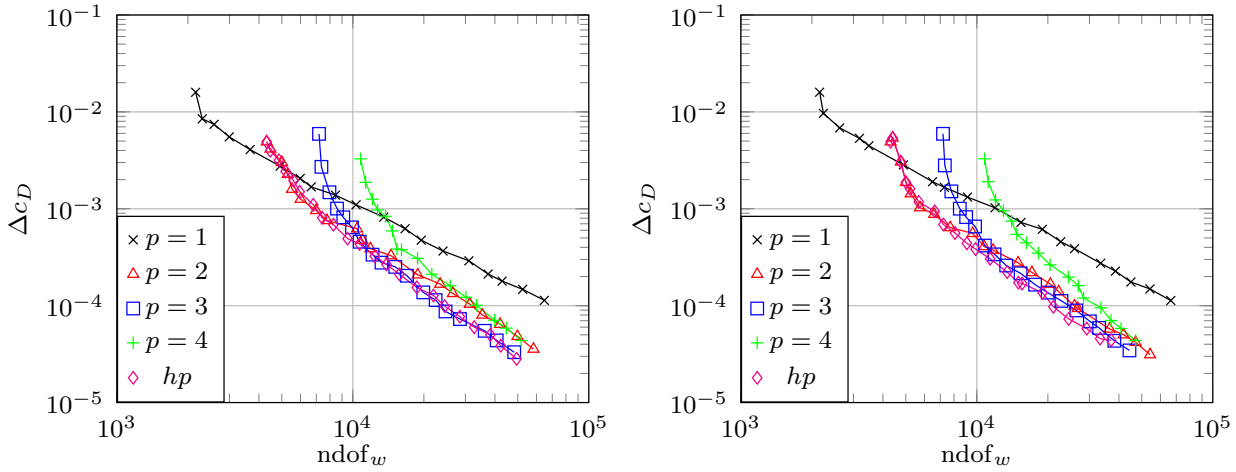

(a) HDG (b) DG

Figure 8: Drag convergence with respect to degrees of freedom ($\text{Ma}_\infty = 0.8$, $\alpha = 1.25°$)

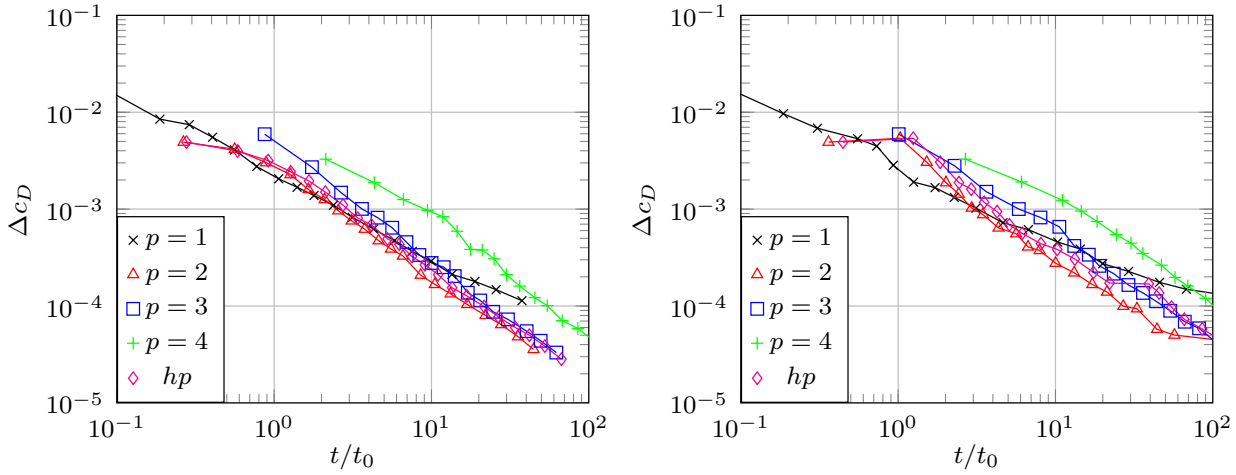

(a) HDG (b) DG

Figure 9: Drag convergence with respect to time ($\text{Ma}_\infty = 0.8$, $\alpha = 1.25°$)

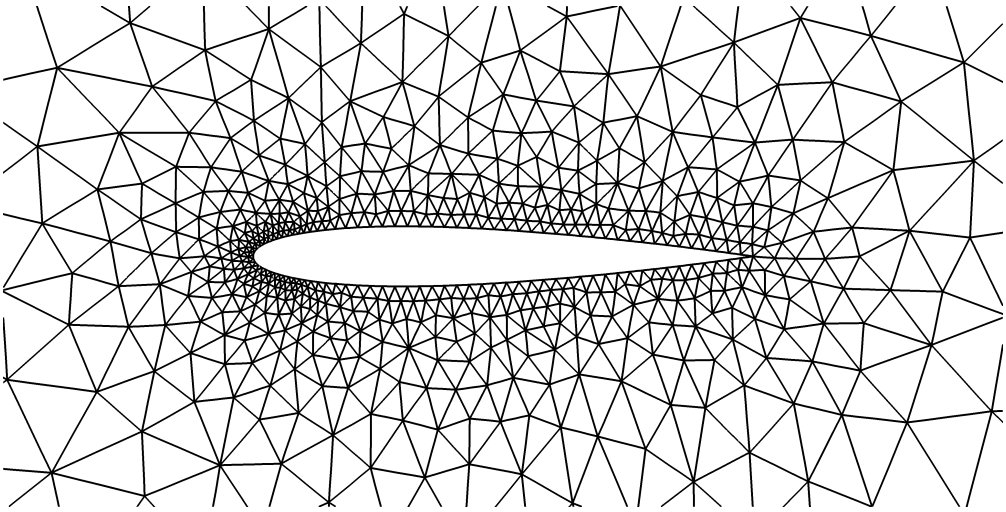

Figure 10: Baseline mesh with 1781 elements for viscous computations

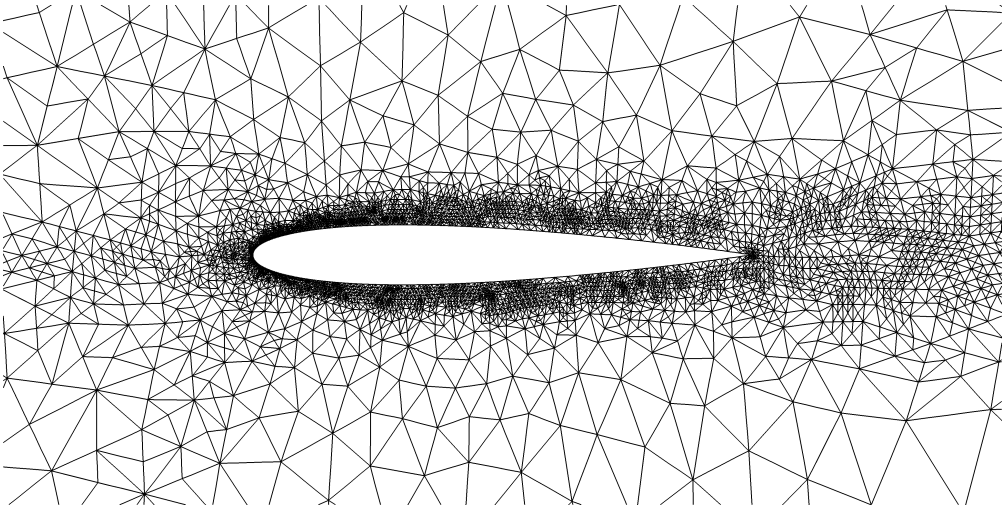

(a) Pure h-adaptation ($p = 2$)

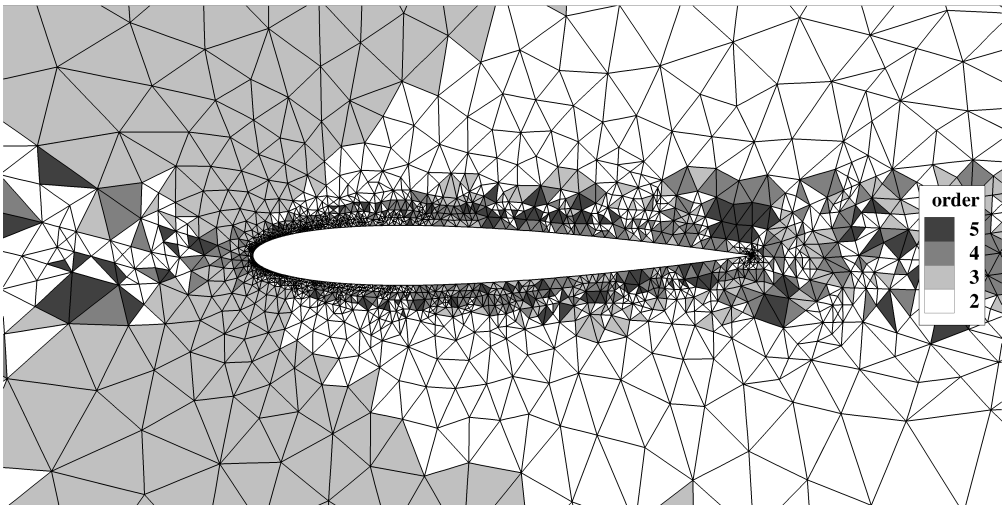

(b) hp-adaptation ($p = 2 \dots 5$)

Figure 11: Adapted meshes for the Navier-Stokes test case ($\mathrm{Ma}_\infty = 0.5$, $\alpha = 1°$, $\mathrm{Re} = 5000$)

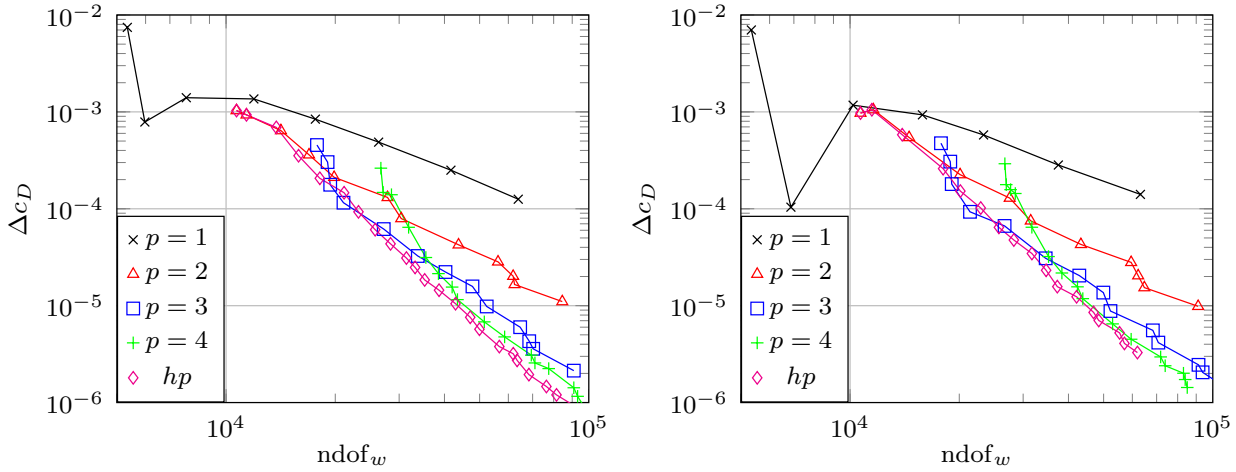

(a) HDG (b) DG

Figure 12: Drag convergence with respect to degrees of freedom ($\text{Ma}_\infty = 0.5$, $\alpha = 1°$, $\text{Re} = 5000$)

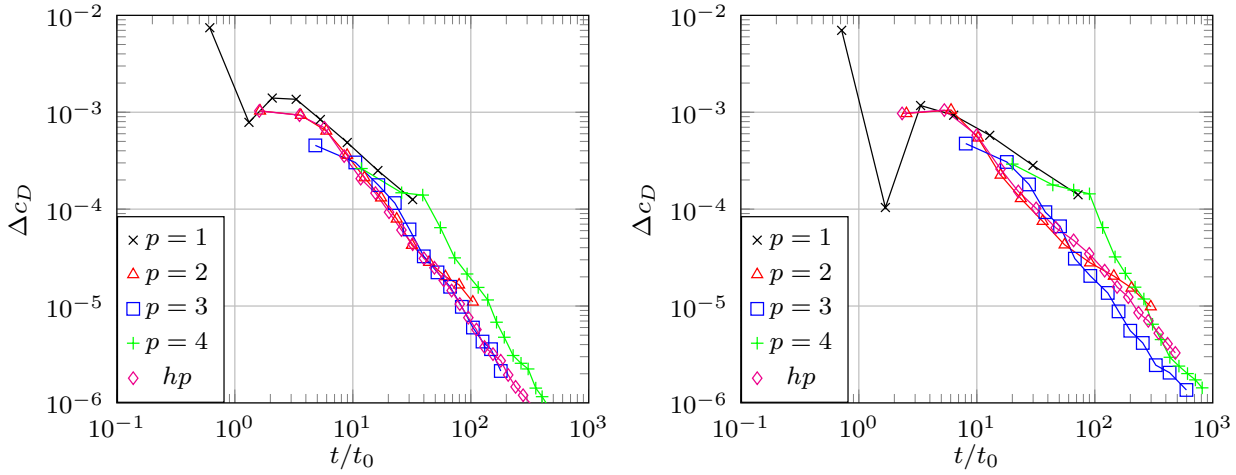

(a) HDG (b) DG

Figure 13: Drag convergence with respect to time ($\text{Ma}_\infty = 0.5$, $\alpha = 1°$, $\text{Re} = 5000$)

References

[1] Aravind Balan, Georg May, and Joachim Schöberl. A stable high-order spectral difference method for hyperbolic conservation laws on triangular elements. *Journal of Computational Physics*, 231(5):2359–2375, 3 2012.

[2] Francesca Iacono and Georg May. Convergence acceleration for simulation of steady-state compressible flows using high-order schemes. AIAA Paper 2009-4132, American Institute of Aeronautics and Astronautics, 2010.

[3] Francesca Iacono, Georg May, and Z. J. Wang. Relaxation techniques for high-order discretizations of steady compressible inviscid flows. AIAA Paper 2010-4991, American Institute of Aeronautics and Astronautics, 2010.

[4] Georg May. On the connection between the Spectral Difference method and the Discontinuous Galerkin method. *Commun. Comput. Phys.*, 4(9):1071–1080, 2011.

[5] Georg May, Francesca Iacono, and Antony Jameson. A hybrid multilevel method for high-order discretization of the euler equations on unstructured meshes. *Journal of Computational Physics*, 229(10):3938–3956, 5 2010.

[6] J. Schütz, M. Woopen, and G. May. A hybridized DG/mixed scheme for nonlinear advection-diffusion systems, including the compressible Navier-Stokes equations. AIAA Paper 12-729, American Institute of Aeronautics and Astronautics, January 2012.

[7] Jochen Schütz and Georg May. An adjoint consistency analysis for a class of hybrid mixed methods. *IMA Journal of Numerical Analysis*, 10 2013.

[8] Jochen Schütz and Georg May. A hybrid mixed method for the compressible navier–stokes equations. *Journal of Computational Physics*, 240(0):58–75, 5 2013.